Materials Science and Engineering A 542 (2012) 21–30

Contents lists available at SciVerse ScienceDirect

Materials Science and Engineering A

journal homepage: www.elsevier.com/locate/msea

Energetics of residual dislocations associated with slip–twin and slip–GBs interactions

Michael D. Sangid [a,*,1], Tawhid Ezaz [b,1], Huseyin Sehitoglu [b]

[a] School of Aeronautics and Astronautics, Purdue University, 701W. Stadium Ave., West Lafayette, IN 47907-2045, USA
[b] Department of Mechanical Science and Engineering, University of Illinois at Urbana-Champaign, 1206W. Green St., Urbana, IL 61801, USA

ARTICLE INFO

Article history:
Received 11 January 2012
Received in revised form 5 February 2012
Accepted 7 February 2012
Available online 15 February 2012

Keywords:
Grain boundary energy
Molecular dynamics simulations (MD simulations)
Residual Burgers vectors
Dislocation
Twins
Grain boundaries (GB)

ABSTRACT

During direct slip transmission of a dislocation through a twin or grain boundary, typically a residual dislocation remains in the boundary plane. Through atomistic simulations, we show systematic cases of slip transmission through various types of ⟨1 1 0⟩ tilts and ⟨1 1 1⟩ twists grain boundaries (GBs). Additionally, one specific type of GB, the coherent twin boundary (CTB), is viewed to investigate the effects of orientation and dislocation type on the slip transmission process. In every case, we measure the residual Burgers vector within the boundary and energy barrier for slip to transmit through the CTB or GB. There exists a direct correlation between the magnitude of the residual Burgers vector and the energy barrier for slip transmission. Hence, in cases of easy slip transmission (i.e. low energy barrier), a small residual dislocation is left in the GB; meanwhile in cases where it is difficult for slip to transmit past the CTB or GB (i.e. high energy barrier), a large residual Burgers vector remains within the boundary.

1. Introduction

Over the last 30 years, research in plasticity has changed scales from investigating a continuum medium to that of the microstructure, i.e. accounting for local heterogeneities in the material. In doing so, the twin and grain boundaries play a critical role in the material, as they strongly influence the strength of the material and also affect the strain incompatibility during plastic deformation by impeding dislocation motion [1]. This behavior is governed by slip–twin and slip–GB interactions. In this paper, we show the energy barrier associated with slip–twin and slip–GB interactions is dependent on the residual dislocation remaining within the twin/GB following the reaction. Further, the information regarding the residual dislocation is crucial for understanding the plastic response of the twin/GB.

In general, there are four possible cases of slip–GB interactions [2]: (i) direct transmission (Fig. 1a), i.e. cross-slip; (ii) direct transmission including residual dislocations in the GB (Fig. 1b); (iii) indirect transmission including residual dislocations in the GB where the incident and outgoing slip systems do not intersect (Fig. 1c), which can be dissociated into a two step process of incorporation of the incident dislocation followed by nucleation of an outgoing dislocation from the GB; and (iv) no transmission—the dislocation is incorporated in the GB (Fig. 1d). The factors that regulate these reactions are the applied stress state, which must be sufficient to drive the incident dislocations past the stress field of the GB [3], the incident dislocation type, the geometry of the GB, and the degree to which the system can relax the local stress concentrations [2]. In the majority of the cases of slip–GB interactions (case ii and iii, above), the incident dislocation, with Burgers vector $\boldsymbol{b_1}$, impinges and reacts with the boundary to produce an outgoing dislocation in the adjacent grain, $\boldsymbol{b_2}$, and a second dislocation that remains in the boundary as a residual dislocation, $\boldsymbol{b_r}$ [4,5].

$$\vec{b}_1 \rightarrow \vec{b}_2 + \vec{b}_r \tag{1}$$

Since $\boldsymbol{b_2}$ is in a different grain from $\boldsymbol{b_1}$, it must be rotated to analyze the Burgers vectors within the same frame. In situ TEM studies provide strong evidence of the dislocation–GB interactions that are experimentally observed [6–10]. In fact, a criterion for slip transmission across GBs was first proposed by Livingston and Chalmers based upon the geometry of the system [11], and later extended by Shen et al. to maximize the resolved shear stress on the outgoing slip system [12]. In 1989, Lee et al. proposed that a third requirement must be satisfied to predict slip transmission, the residual dislocation in the grain boundary be minimized [13].

The GBs act as strong barriers to impede dislocation motion, thus requiring an increase in external stress for slip transmission

* Corresponding author. Tel.: +1 765 494 0146; fax: +1 765 494 0307.
E-mail address: msangid@purdue.edu (M.D. Sangid).
[1] These authors contributed equally to writing this manuscript.

0921-5093/$ – see front matter © 2012 Elsevier B.V. All rights reserved.
doi:10.1016/j.msea.2012.02.023

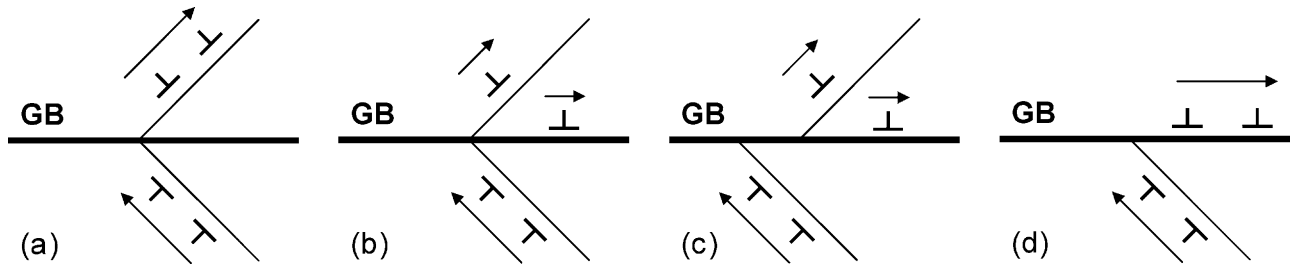

Fig. 1. Schematic of slip–GB interaction cases: (a) direct transmission, where the dislocation penetrates into the adjacent grain, i.e. cross-slip, (b) direct transmission, where the dislocation dissociates into slip in the adjacent grain and a residual dislocation remaining within the GB, (c) indirect transmission where the incident and outgoing slip planes do not intersect, also including a residual dislocation within the GB (a two step process of the dislocation being incorporated within the GB followed by slip nucleating from the GB into the adjacent grain), and (d) no transmission, where the dislocations are incorporated within the GB.
These schematics are redrawn from Ref. [2].

[14,15]. In most cases, $|\boldsymbol{b_1}| = |\boldsymbol{b_2}|$, and the energy barrier to this reaction is proportional to the self-energy of the residual dislocation left behind in the boundary [2]. Upon subsequent reactions of dislocations with the twin/grain boundary, a high density of residual dislocations accumulates within the boundary, in essence acting to work harden the boundary, increase the energy barrier, and resist further slip transmission leading to a pile-up of dislocations at the twin/grain boundary, as shown by Jacques [16] and Baillin et al. [17]. Thus, by understanding the character of the residual dislocation, as presented in this paper, we can effectively understand the plastic response of the GB.

In recent years, two strategies are employed in modeling the residual dislocations resulting from slip–twin and slip–GB: (i) analysis of the deformation fields within and across grains [18–20] and (ii) atomistic simulations [21,22]. As a dislocation glides within a single crystal, the lattice becomes curved [23]. With this in mind, Gurtin and Needleman developed a gradient theory of single-crystal plasticity that accounts for the Burgers vector from the curl of the plastic distortion field [18]. Beaudoin et al. implemented a novel jump condition into a mesoscale field dislocation mechanics model [19], thus allowing the Burgers vector to be conserved through lattice rotations during dislocation interactions with GBs in a crystal plasticity formulation [20]. Another approach is to start at the defect level using atomistic simulations, namely molecular dynamics (MD). MD simulations of slip–GB interactions provide analysis of the residual dislocations [21,22]. In both approaches, the residual dislocation is a byproduct of the compatibility constraints of the lattice and deformation field and do not explicitly measure the energy barriers for these reactions.

Recently, Ezaz et al. [24] investigated slip–twin interaction in Cu and Sangid et al. [25] investigated slip–GB interaction in Ni via MD simulations. By using techniques explained in Section 2, the activation energies for the dislocation reactions are calculated in their studies. Thus, in this paper, we systematically measure the energy profile of an outgoing dislocation ($\boldsymbol{b_2}$) in the presence of a residual dislocation ($\boldsymbol{b_r}$) at the twin or grain boundary in Cu and Ni. The peak energy (termed as the unstable stacking fault energy) for several energy profiles of an outgoing dislocation ($\boldsymbol{b_2}$) are compared with the magnitudes of the residual dislocation ($\boldsymbol{b_r}$) produced and the associated reaction at the boundary. The energy profiles are normalized against its glide plane area such that it can be compared with the well-established generalized planar fault energy (GSFE). We analyze two different materials with high (Ni) and low (Cu) stacking fault energies to show that this trend holds in various material systems regardless of the material's slip character. From this analysis, we calculate the energy barrier to slip and also make estimates on the subsequent energy barriers to further slip. This information is vital to understanding the individual strength of each twin/grain boundary, which ultimately leads to the hardening response of the material.

2. Molecular dynamics simulations

Molecular dynamics simulations are employed to study the slip–twin and slip–GB interactions in the form of a Sandia code called LAMMPs [26,27]. Embedded atom method (EAM) potentials are chosen to match the stacking fault energies of the material. The Mishin EAM Cu potential [28] results in an intrinsic and unstable stacking fault energies of γ_{ISF}-44 mJ/m^2 and γ_{US}-167 mJ/m^2, respectively, while the Foiles–Hoyt EAM Ni [29] potential results in γ_{ISF}-127 mJ/m^2 and γ_{US}-255 mJ/m^2. Both potentials are in agreement with experiments [3,30] and the generalized stacking fault energies (GSFE) and generalized planar fault energies (GPFE) determined by ab initio calculations [30,31] (as shown in Table 1), including the unstable γ_{US}, which is especially important in simulating dislocation mechanics [32]. A physical description of the GSFE and GPFE formations in FCC metals is given in Appendix A. The system set-up and MD parameters are given in full detail for the Cu slip–twin and Ni slip–GB interactions in [24,25], which the reader is referred to for more information. A summary of the MD methods is presented as follows.

The simulation box is set-up maintaining periodic boundary condition in all three directions. For the cases of the Ni slip–GB interactions, the GBs are constructed according to the axis–angle pair description, maintaining periodic boundary conditions, and subjected to uniaxial tension loading as shown in Table 2 and Fig. 2a. The simulations do not employ fixed regions in the cell, hence atoms are free to move as long as it is energetically favorable. Periodic boundary conditions suppress rigid body translations between the two crystals, so the GB structure may be slightly less stable than typical boundaries. We expect that this contributes to only minor deviations in the material response of the GB, as the static GB energies in our simulations are in agreement with available GB

Table 1
Generalized planar fault energies (in units of mJ/m^2) calculated from EAM interatomic potentials for Cu and Ni compared with values from experiments and ab initio calculations in the form of density functional theory (DFT).

Metal	Analysis technique	γ_{US}	γ_{ISF}	γ_{UT}	$2\gamma_{TSF}$
Cu	EAM potential[a]	167	44	187	42
	DFT[b]	180	41	200	40
	Experiment[c]	–	45	–	48
Ni	EAM potential[d]	255	127	318	126
	DFT[e]	273	110	324	110
	Experiment[c,e]	–	125	–	86

[a] MD from this study using the Mishin EAM Cu potential [28].
[b] Density functional theory (DFT) VASP–PAW–GGA fault energies for Cu from Ref. [31].
[c] Experimental fault energies from Table A-1 of Ref. [3].
[d] MD from this study using the Foiles–Hoyt EAM Ni potential [29].
[e] Density functional theory (DFT) VASP–GGA fault energies for Ni from Ref. [30].

Table 2
Summary of different slip–twin interactions addressed in this article and their respective energy barriers at the twin boundary. All the slip systems are in the coordinate frame of grain 1. The residual dislocation magnitudes are expressed in terms of, *a*, the lattice constant of Cu.

Loading orientation	Schmid factor on twin system	Incident leading dislocation	Outgoing dislocation	Residual dislocation	Magnitude of residual dislocation	Angle between incident and outgoing	Unstable energy barrier (γ_{UT}) (mJ/m^2)
[0 1 0]	0.24	$\frac{a}{6}[\bar{1}12](\bar{1}\,1\,\bar{1})$	$\frac{a}{6}[\bar{1}\,2\,1](\bar{1}\,\bar{1}\,1)$	$\frac{a}{6}[0\,\bar{1}\,1]$	0.24a[a]	33.56°	199
[0 1 0]	0.24	$\frac{a}{6}[2\,1\,\bar{1}](\bar{1}\,1\,\bar{1})$	$\frac{a}{6}[2\,\bar{1}\,\bar{1}](1\,1\,1)$	$\frac{a}{3}[0\,1\,0]$	0.32a[b]	48.12°	212
[1 1 1]	0.31	$\frac{a}{6}[1\;\;1\,2](1\,\bar{1}\,\bar{1})$	$\frac{a}{6}[1\,2\,\bar{1}](1\,\bar{1}\,\bar{1})$	$\frac{a}{6}[0\,\bar{1}\,3]$	0.53a[a]	80.41°	232

[a] Incorporation and blockage.
[b] Incorporation and transmission.

values from the literature [33]. For the cases of the Cu slip–twin interactions, the system is then rotated to the appropriate loading direction and subjected to a uniaxial tension loading as shown in Table 2. For cases when periodicity cannot be invoked due to the geometry of twin boundaries as shown in Fig. 2b, we ensure that the box size is chosen to achieve convergence of results without effects from the free surfaces. For all cases, a void is introduced into the simulation box to facilitate dislocation nucleation, in order to simulate a single dislocation interacting with the twin/grain boundary. After insertion of the void, the system is statically and dynamically relaxed using an *NPT* ensemble where the number of atoms in the simulation box, *N*, the pressure in the three directions (stress

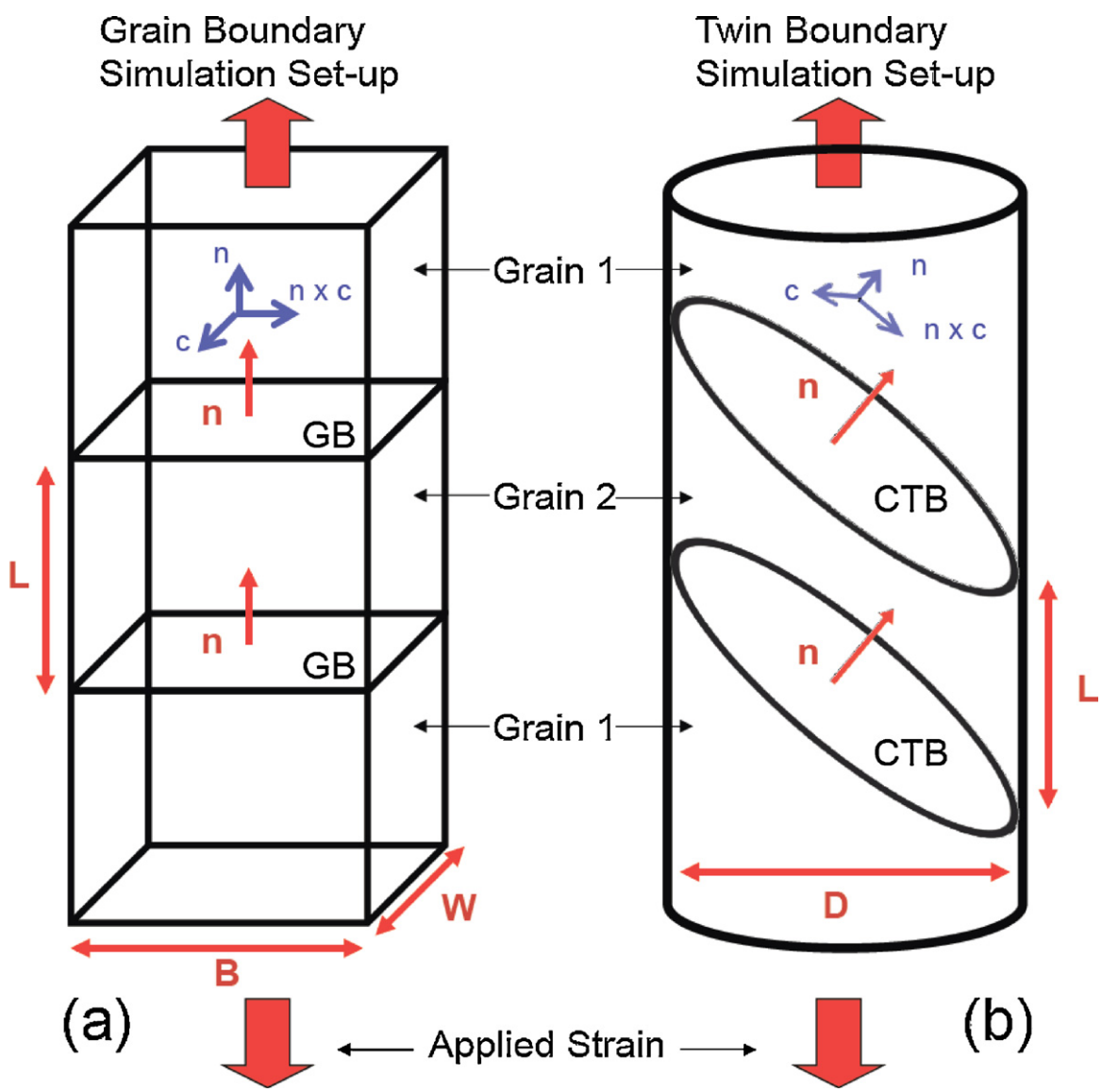

Fig. 2. Schematic of the set-up for the atomic simulation displaying a pair of GBs or CTBs. (a) For the GB simulations, periodic boundary conditions (PBCs) are enforced in all three dimensions and the box dimensions (*L*, *B*, *W*) are chosen to satisfy the PBCs. The axis of rotation for tilt and twist GBS is *c* and *n*, respectively. (b) For the twin boundary simulations, PBCs are enforced only in the vertical direction, representing a nano-wire. The twin is 10 layers thick and the wire diameter, *D*, is sufficiently large to ensure the dislocation reaction occurs at the core of the wire and the free surfaces do not effect the dislocation reactions. For both sets of simulations, the normal to the GB, *n*, represents the boundary plane and the distance between boundaries, *L*, is sufficiently large to avoid boundary–boundary interactions.

free boundaries), P, and the system temperature, T (10 K), are held constant throughout the simulation.

Special codes are written to visualize the details of the dislocation–CTB/GB interactions with visual molecular dynamics (VMD) [34], an atomistic configuration viewer program. The centro-symmetry parameter (CSP) [35] is utilized to locate and color the defects within the material based on its position with respect to its nearest neighbors (blue indicates a partial dislocation, while white denotes a stacking fault). For clarity of presentation, defect-free atoms that do not participate in the interaction are deleted from the MD simulation snapshots.

Dislocation transmission energy barriers at the boundary are calculated from the potential energy difference between gliding atoms and the perfect lattices at a particular time step. For coplanar boundaries, i.e. the CTB, an MD-based short range planar energy calculation method [24] is utilized to monitor an array of atoms on the dislocation glide plane at a time step of 0.01 fs. Glide direction of the atoms in front of the dislocation is obtained with a Burgers circuit code. This is crucial for precise calculation of the interfacial area swept by the gliding atoms. The energies per unit area of GSFE or GPFE are then obtained by normalizing the energy barriers with the interface area. We point out that the energy profile presented using this method is independent of the length scale and relies on the glide plane and direction of the dislocation. In this study, the energies of the locally tracked atoms are normalized with the area of the nearest neighbor atoms within the glide plane. The image force contributions were checked by varying the simulation cell size and found to be insignificant. For non-coplanar boundaries, a control box is utilized to record the energy of the atoms ahead of the dislocation as it interacts with the boundary of interest, in order to measure the energy barrier for slip transmission [25].

Throughout the dynamics calculations, the temperature of the system is maintained at 10 K; hence providing a consistent baseline. Internal energy fluctuation of the monitored atoms due to entropy is measured to be very small at this temperature, on the order of 0.0011 eV. The long-range hydrostatic stress field is removed from the energy calculation by comparing the energy of perfect FCC atoms under the same external stress field. This provides a consistent framework for comparison of GSFE/GPFE and points any deviation of γ_{US} or γ_{UT} to the effect of the internal local stresses nearby the local boundaries. This method was validated by comparisons with the baseline GSFE, which provided excellent agreement [25]. Further, this method allows quantitative calculation of the energy barriers for slip transmission, which is used in Sections 3 and 4 to compare each case with its resistance to dislocation motion.

3. Results

In this section, we present results from a systematic series of MD simulations to calculate the residual dislocations within the boundary produced by slip–twin and slip–GB interactions. We start by analyzing one specific type of GB, the coherent twin boundary ($\Sigma 3$ GB). In the slip–twin interactions, we study the effect of the type of incident dislocation and loading configuration (i.e. stress-state at the twin boundary) on the residual Burgers vector and consequently energy barrier for slip transmission. From there, we generalize the type of GB, which we demarcate based on the character of GB.

3.1. Residual Burgers vector of slip–twin interaction

In this present section, three cases of slip–twin interactions are investigated to calculate the resulting residual Burgers vector, which allows us to study the effects of two variables: loading orientations, [1 1 1] and [0 1 0], (i.e. stress-state at the twin boundary) and type of the incident dislocation tested with the case of the [010] orientation. Two different loading orientations, [1 1 1] and [0 1 0], are selected to monitor the dislocation-twin boundary interaction and identify the influence of the residual dislocation on the glide energy barrier. These loading orientations are picked based on the relative resolved shear stress on the leading and trailing partials of the incident dislocations and the number of systems with maximum Schmid factor. In both the cases, a preexisting 10 layer twin is placed inside the crystal, in a way that the resolved shear stress on that CTB is maximized. Here we note that, for the [0 1 0] loading, the trailing partial has a Schmid factor even higher than the leading partial, which inactivates this system for the deformation twin. Therefore, for the [0 1 0] orientation, we consider non-deformation twins only, which originates during annealing or growth processes, whereas for the case of the [1 1 1] orientation, the twin is considered a deformation twin. A third case is chosen for the same [0 1 0] orientation, whereas a different type of incident dislocation interacts with the twin boundary.

First, upon tensile loading in the [0 1 0] crystal orientation, two mechanisms are operative depending on the geometry of the incident dislocation and CTB. In the first mechanism, an incorporation of the twinning partial followed by a complete blockage is observed. The incident dislocation reacts with a $(\bar{1}\,1\,\bar{1})[\bar{1}\,1\,2]$ CTB, which has the maximum twin Schmid factor for the [0 1 0] loading orientation. This is shown in Fig. 3a, where the leading and trailing bowed partials are noted. The incident dislocation is a 60° mixed dislocation type with a 30° leading and a 90° trailing partial based on a Burgers circuit analysis. The leading 30° partial glides in the $a/6[\bar{1}\,1\,2]$ direction on the $(\bar{1}\,1\,\bar{1})$ plane as it leaves a widening intrinsic stacking fault behind. The Burgers vector of the dislocation is invariant along the dislocation line, although the character of dislocation changes along the dislocation front. At the line of intersection, the 30° leading partial is found to have screw and edge components of $a/4[0\,1\,1]$ and $a/12[\bar{2}\,\bar{1}\,1]$, respectively. This can be summarized in Eq. (2).

$$\underset{\text{Edge}}{\frac{a}{12}[\bar{2}\,\bar{1}\,1]} + \underset{\text{Screw}}{\frac{a}{4}[0\,1\,1]} \rightarrow \underset{30^\circ\text{ leading partial}}{\frac{a}{6}[\bar{1}\,1\,2]} \tag{2}$$

A 90° trailing partial follows the leading partial, $a/6[\bar{2}\,\bar{1}\,1](\bar{1}\,1\,\bar{1})$, as noted in Fig. 3a. Once the 30° leading partial with a $a/6[2\,1\,\bar{1}]$ Burgers vector is incorporated in the deformation CTB, the $a/6[0\,\bar{1}\,1]$ (magnitude 0.23a, where a is the lattice constant of Cu) type stair-rod dislocation is generated along with a $a/6[\bar{1}\,2\,1]$ twinning partial at the CTB, as shown in Fig. 3b. The $a/6[\bar{1}\,2\,1](\bar{1}\,\bar{1}\,1)$ twin system has the maximum Schmid factor for the [0 1 0] loading direction and is thus favorable for glide. This twinning partial glides along the CTB, and thus causes an increase in the transverse thickness of the twin lamella according to the following reaction:

$$\underset{\text{Leading partial}}{\frac{a}{6}[\bar{1}12]} \rightarrow \underset{\text{Twinning partial}}{\frac{a}{6}[\bar{1}21]} + \underset{\text{Stair rod dislocation}}{\frac{a}{6}[0\bar{1}1]} \tag{3}$$

which is also summarized in Table 2. The unstable energy barrier (γ_{UT}) for nucleating the $a/6[\bar{1}\,2\,1]$ twinning partial in the presence of a $a/6[0\,\bar{1}\,1]$ residual dislocation is calculated and found to be 199 mJ/m^2. When the trailing partial $a/6[\bar{2}\,\bar{1}\,1]$ reacts with the stair-rod, this causes nucleation of a stable Frank partial dislocation at the intersection, see Fig. 3c. This can be summarized as follows (in Table 2).

$$\underset{\text{Stair rod}}{\frac{a}{6}[0\bar{1}1]} + \underset{\text{Trailing partial}}{\frac{a}{6}[\bar{2}\bar{1}1]} \rightarrow \underset{\text{Frank dislocation}}{\frac{a}{3}[\bar{1}\bar{1}1]} \tag{4}$$

The Frank dislocation (Eq. (4)) is a sessile imperfect dislocation and its Burgers vector is directed normal to the {1 1 1} plane.

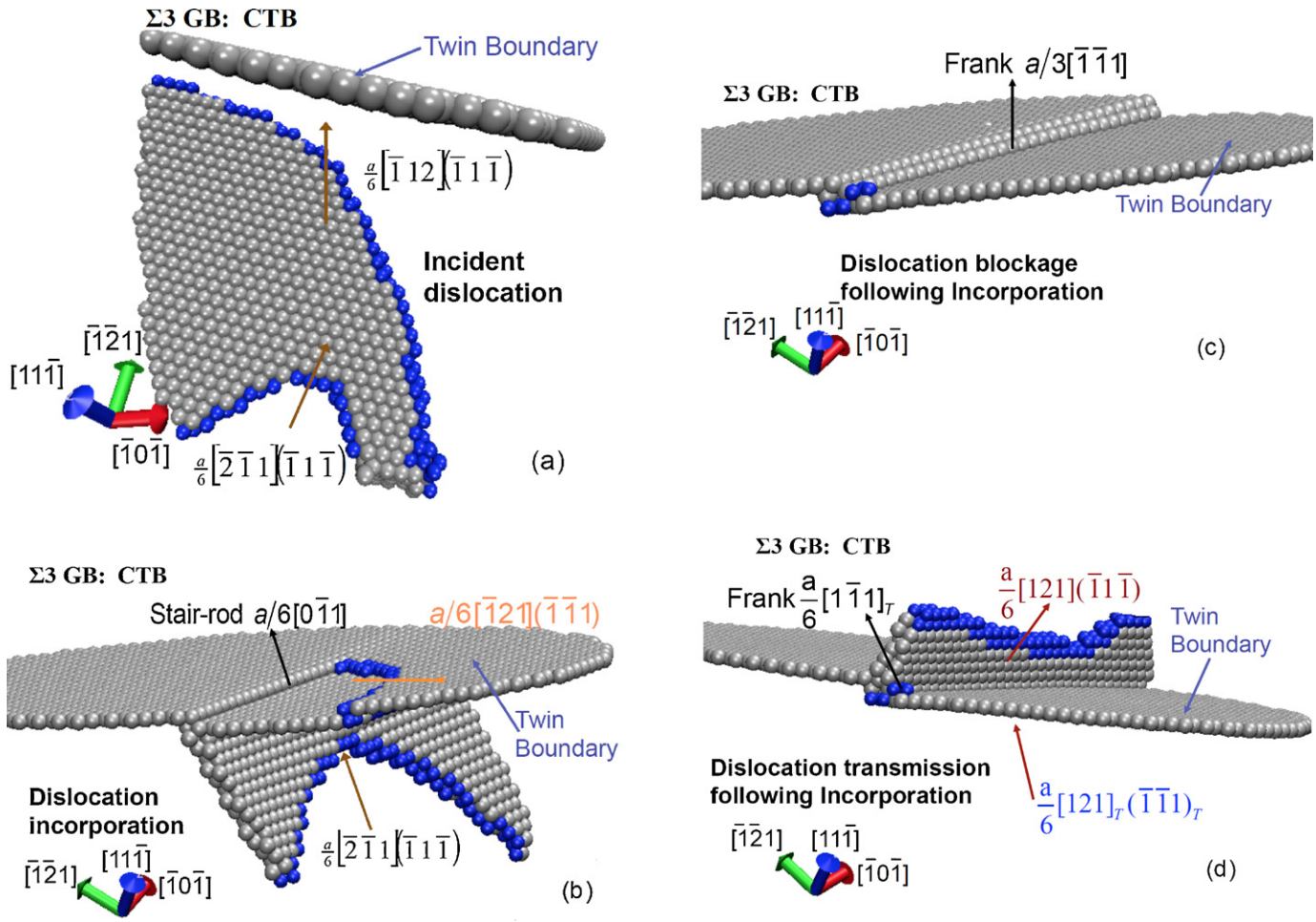

Fig. 3. Snapshots of dislocation–twin boundary interaction for the [0 1 0] loading direction in tension displaying the slip transmission events: (a) impinging 60° dislocation with a $a/6[\bar{1}\,1\,2]$ 30° leading and $a/6[2\,\bar{1}\,1]$ 90° trailing partial dislocation glides through the matrix before interaction. (b) After the leading partial interacts with the twin boundary, a twinning partial $a/6[\bar{1}\,2\,1]$ and a sessile stair-rod $a/6[0\,\bar{1}\,1]$ nucleates at the intersection. (c) A sessile Frank partial generated at the boundary, once the trailing partial interacts with the boundary. (d) A dislocation transmission case is shown, where the dislocation moves to the twinned region $a/6[1\,2\,1]_T(\bar{1}\,\bar{1}\,1)_T$ once the trailing partial $a/6[1\,2\,1](\bar{1}\,1\,\bar{1})$ interact with the boundary. The view points are slightly varied for a clearer comprehension of the event.

Next, a second dislocation–twin boundary interaction mechanism is observed in the same [0 1 0] loading orientation, once a $a/6[2\,1\,\bar{1}](\bar{1}\,1\,\bar{1})$ dislocation interacts with a (1 1 1) twin boundary. In this case, a twin boundary incorporation of the incident dislocation results in transverse twin growth of the lamella followed by a transmission of the dislocation inside the twinned region, as shown in Fig. 3d. During the incorporation process, a twinning partial, $a/6[2\,\bar{1}\,\bar{1}](1\,1\,1)$, is nucleated after the interaction, which glides and increase the twin thickness in the same manner as discuss above. However, the incident dislocation leaves a $a/3[0\,1\,0]$ residual stair-rod dislocation of magnitude 0.33a at the interaction site. The reaction of this interaction is displayed in Table 2. The unstable energy barrier (γ_{UT}) for nucleating the $a/6[2\,\bar{1}\,\bar{1}]$ twinning partial in the presence of a $a/3[0\,1\,0]$ residual dislocation is measured to be 212 mJ/m^2.

When the trailing partial $a/6[1\,2\,1]$ reacts with the stair-rod dislocation, it causes nucleation of a glissile partial penetrating the twin and a Frank partial dislocation at the intersection. This can be summarized as follows:

$$\underset{\text{Stair rod}}{\frac{a}{3}[010]} + \underset{\text{Trailing partial}}{\frac{a}{6}[121]} \rightarrow \underset{\text{Glissile dislocation}}{\frac{a}{6}[121]_T} + \underset{\text{Frank dislocation}}{\frac{a}{6}[1\bar{1}1]_T} \quad (5)$$

The $a/6[1\,2\,1]_T$ penetrates the twin as it glides on the $(\bar{1}\,\bar{1}\,1)_T$ plane leaving a sessile Frank dislocation at the interaction site. The unstable energy barrier (γ_{US}) during nucleation of the $a/6[1\,2\,1]_T$ dislocation in the presence of this Frank dislocation is measured to be 312 mJ/m^2.

Thirdly, the [1 1 1] tensile loading orientation results in dislocation incorporation in the twin without any transmission inside the twin. Only the leading partial is observed in this orientation. The leading partial glides on the $(\bar{1}\,\bar{1}\,1)$ plane in the $a/6[1\,1\,2]$ direction creating an angle of 30° with the line of intersection of the CTB. The non-screw component, upon impinging at a $(1\,\bar{1}\,\bar{1})[\bar{1}\,\bar{2}\,1]$ CTB, nucleates a twinning dislocation along the CTB, which increases the twin lamella by one layer. In the process, a stair-rod dislocation is generated according to the following.

$$\underset{\text{Leading partial}}{\frac{a}{6}[1\,1\,2]} \rightarrow \underset{\text{Twinning partial}}{\frac{a}{6}[1\,2\,\bar{1}]} + \underset{\text{Stair rod dislocation}}{\frac{a}{6}[0\,\bar{1}\,3]} \quad (6)$$

Note that, nucleation of a $a/6[0\,\bar{1}\,3]$ stair-rod is of different magnitude (0.527a) than the $a/3[0\,1\,0]$ and $a/6[0\,\bar{1}\,1]$ cases discussed earlier. The stair-rod dislocation does not dissociate and remains sessile at the interaction site. The γ_{UT} of magnitude 232 mJ/m^2 was obtained for this loading orientation, which is higher than the previous cases and the baseline γ_{UT} levels. This difference in magnitude has an important implication on the hardening behavior of

Table 3
Results of the various cases of slip–GB interactions, including the characterization of the GB (axis-angle pair and CSL Σ value), interfacial GB energy, and during slip transmission the: energy barrier, active slip system of incident and outgoing dislocation, and the residual Burgers vector (direction out of the GB plane and magnitude).

GB description		Sigma value	Static GB energy (mJ/m^2)	Slip–GB energy barrier (mJ/m^2)	Incident dislocation	Outgoing dislocation	Residual Burgers vector	Residual Burgers vector magnitude
Axis	Angle							
[1 1 0]	0.00°	1	0.0	254.4	$\frac{a}{6}[2\,1\,1]_1(1\,\bar{1}\,\bar{1})_1$	$\frac{a}{6}[2\,1\,1]_2(1\,\bar{1}\,\bar{1})_2$	–	0.00a
[1 1 0]	38.94°	9	961.5	330.0	$\frac{a}{6}[2\,1\,1]_1(1\,\bar{1}\,\bar{1})_1$	$\frac{a}{6}[1\,\bar{1}\,2]_2(1\,\bar{1}\,\bar{1})_2$	$\frac{2a}{27}[\bar{2}\,\bar{2}\,1]_1(1\,1\,4)_1$	0.22a
[1 1 0]	86.63°	17	923.7	351.8	$\frac{a}{6}[2\,1\,1]_1(1\,\bar{1}\,\bar{1})_1$	$\frac{a}{6}[1\,2\,1]_2(\bar{1}\,1\,\bar{1})_2$	$\frac{5a}{102}[3\,3\,\bar{4}]_1(2\,2\,3)_1$	0.29a
[1 1 0]	50.48°	11	438.6	511.2	$\frac{a}{6}[2\,1\,1]_1(1\,\bar{1}\,\bar{1})_1$	$\frac{a}{6}[1\,\bar{1}\,2]_2(1\,\bar{1}\,\bar{1})_2$	$\frac{a}{22}[7\,\bar{4}\,\bar{1}]_1(1\,1\,3)_1$	0.37a
[1 1 1]	0.00°	1	0.0	254.4	$\frac{a}{6}[2\,1\,1]_1(1\,\bar{1}\,\bar{1})_1$	$\frac{a}{6}[2\,1\,1]_2(1\,\bar{1}\,\bar{1})_2$	–	0.00a
[1 1 1]	21.80°	21	526.3	319.0	$\frac{a}{6}[2\,1\,1]_1(1\,\bar{1}\,\bar{1})_1$	$\frac{a}{6}[1\,1\,2]_2(\bar{1}\,\bar{1}\,1)_2$	$\frac{5a}{126}[5\,\bar{1}\,\bar{4}]_1(1\,1\,1)_1$	0.26a
[1 1 1]	27.80°	13	504.8	327.0	$\frac{a}{6}[1\,1\,2]_1(\bar{1}\,\bar{1}\,1)_1$	$\frac{a}{6}[1\,1\,2]_2(\bar{1}\,\bar{1}\,1)_2$	$\frac{2A}{39}[\bar{3}\,\bar{1}\,4]_1(1\,1\,1)_1$	0.26a
[1 1 1]	38.20°	7	525.8	336.6	$\frac{a}{6}[2\,1\,1]_1(1\,\bar{1}\,\bar{1})_1$	$\frac{a}{6}[1\,\bar{1}\,2]_2(1\,\bar{1}\,\bar{1})_2$	$\frac{a}{6}[1\,\bar{1}\,2]_1(1\,1\,1)_1$	0.41a

the material as it indicates a different local energy field resulting in a different barrier for the twinning partial's nucleation.

3.2. Residual Burgers vector of slip–GB interaction

Six distinct GBs are constructed to study the slip–GB interaction in Ni. Through an axis-angle pair description of the GB, 38.94°, 50.48°, and 86.63° tilts around the ⟨1 1 0⟩ axis resulted in Σ9, 11, and 17 GBs; while 38.2°, 27.8°, and 21.8° twists around the ⟨1 1 1⟩ axis resulted in Σ7, 13, and 21 GBs. Each of these GBs is compared with the case of a perfect FCC crystal, which corresponds to a 0° rotation denoted as a Σ1 GB. Originally, each system is statically relaxed via the conjugant gradient method and its GB energy is measured, as shown in Table 3. As expected the perfect FCC configuration has 0 GB energy, since no GB is present, no defects exists. It can be seen that the Σ11 GB has a low GB energy corresponding to a stable structure and a low defect concentration at the GB; meanwhile the Σ9 and 17 GBs, have a complex defect structure at the GB and therefore a relatively high GB energy [33].

An incident dislocation is introduced in each simulation as the direction is indicated in Table 3. In each simulation, the incident dislocation reacts with the GB and the outgoing dislocation is measured. Examples of the reactions for slip–Σ11 GB and slip–Σ7 GB interactions are shown in Fig. 4a and b, respectively. As expected, in all cases reported in Table 3, both the incoming and outgoing dislocations are located on {1 1 1} closed pack planes in ⟨1 1 2⟩ partial directions. From these dislocations, the residual Burgers vector, $\boldsymbol{b_r}$, is measured:

$$\vec{b}_r = \vec{b}_{in} - R'_{12} \cdot \vec{b}_{out} \tag{7}$$

where $\boldsymbol{R_{12}}$ is the misorientation tensor between grains 1 and 2. The $\boldsymbol{b_r}$ is calculated from the difference in the dislocation directions during the reaction, since it is difficult to accurately measure the residual dislocation from a Burgers circuit algorithm due to the complex structural units that compose the GB [36,37]. The calculated $\boldsymbol{b_r}$ (vector and magnitude) and energy barrier for slip transmission (as discussed in Section 2) for each type of GB is shown in Table 3.

We first analyze three types of [1 1 0] tilt GBs. The 38.94°/[1 1 0] (Σ9) GB is constructed with a complex defect structure at the GB possessing a static GB energy of 961.5 mJ/m^2. For this system, a dislocation on the $a/6[2\,1\,1]_1(1\,\bar{1}\,\bar{1})_1$ slip system interacts with the GB resulting in an outgoing dislocation on the $a/6[1\,\bar{1}\,2]_2(1\,\bar{1}\,\bar{1})_2$ slip system and a residual dislocation, $2a/27[\bar{2}\,\bar{2}\,1]_1(1\,1\,4)_1$, of magnitude 0.22a (where a is the lattice constant of FCC Ni). This slip–Σ9 GB reaction results in an energy barrier of 330.0 mJ/m^2. A similar type of GB is the 86.63°/[1 1 0] (Σ17) GB, which has a static GB energy of 923.7 mJ/m^2. During slip–Σ17 GB interaction, an incident $a/6[2\,1\,1]_1(1\,\bar{1}\,\bar{1})_1$ dislocation reacts with the Σ17 GB, thus overcoming an energy barrier of 351.8 mJ/m^2 to produce an outgoing $a/6[1\,2\,1]_2(\bar{1}\,1\,\bar{1})_2$ dislocation, a $\boldsymbol{b_r}$ of $5a/102[3\,3\,\bar{4}]_1(2\,2\,3)_1$, and a $|\boldsymbol{b_r}|$ of 0.29a. Meanwhile, a 50.48°/[110] (Σ11) GB has a simple defect structure at the GB and a corresponding relatively low static GB energy of 438.6 mJ/m^2. The slip–Σ11 GB reaction is shown in Fig. 4a and results in a

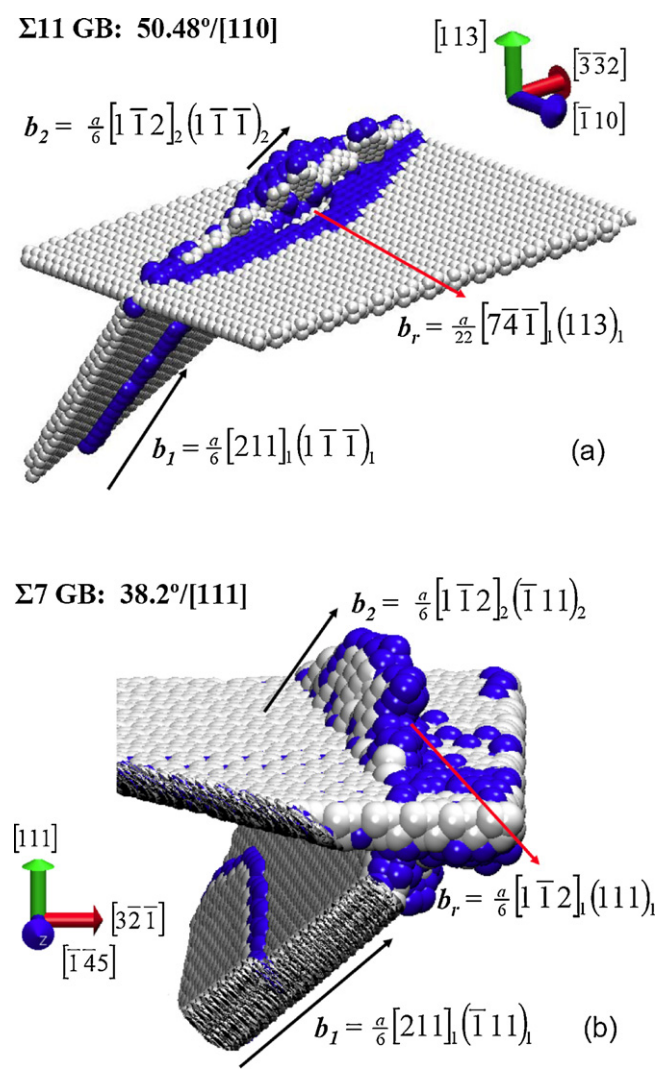

Fig. 4. Atomistic snapshots of the slip transmission process through (a) Σ11 GB (50.48°/[1 1 0]), where the residual Burgers vector is visible within the GB shown as a dislocation loop (blue atoms); and (b) Σ7 GB (38.2°/[1 1 1]), where the residual Burgers vector is a step or ledge at the GB, although due to the complex structure of the GB, it is not readily apparent. In each reaction, the incoming and outgoing dislocations (with directions) are clearly shown.

relatively high energy barrier for slip transmission, 511.2 mJ/m^2, as an incident $a/6[2\,1\,1]_1(1\,\bar{1}\,\bar{1})_1$ dislocation produces an outgoing $a/6[1\,\bar{1}\,2]_2(1\,\bar{1}\,\bar{1})_2$ dislocation, a residual $a/22[7\,\bar{4}\,\bar{1}]_1(1\,1\,3)_1$ dislocation, and a relatively high $|\boldsymbol{b_r}|$ of 0.37a.

Next, we analyze three cases of [1 1 1] twists GBs. All three of these GBs are similar in structure. As the 21.8°/[1 1 1] (Σ21) GB, 27.8°/[1 1 1] (Σ13) GB, and 38.2°/[1 1 1] (Σ7) GB produce static GB energies of 526.3, 504.8, and 525.8 mJ/m^2, respectively. Consequently, all the energy barriers for slip transmission through the Σ21, 13, and 7 GBs are similar, 319.0, 327.0, and 336.6 mJ/m^2, respectively. The cases of the Σ21 and 13 GBs are analogous to one another, as the $a/6[2\,1\,1]_1(1\,\bar{1}\,\bar{1})_1$ dislocation–Σ21 GB and $a/6[1\,1\,2]_1(\bar{1}\,\bar{1}\,1)_1$ dislocation–Σ13 GB interactions result in the same active outgoing $a/6[1\,1\,2]_2(\bar{1}\,\bar{1}\,1)_2$ slip system and similar magnitudes of the residual Burgers vector with a value of 0.26a, while the actual residual Burgers vectors are different, $5a/126[5\,\bar{1}\,\bar{4}]_1(1\,1\,1)_1$ and $2a/39[\bar{3}\,\bar{1}\,4]_1(1\,1\,1)_1$, respectively. Comparatively, the Σ7 GB has a slightly higher energy barrier for slip transmission, 336.6 mJ/m^2, as an incident $a/6[2\,1\,1]_1(1\,\bar{1}\,\bar{1})_1$ dislocation produces an outgoing $a/6[1\,\bar{1}\,2]_2(1\,\bar{1}\,\bar{1})_2$ dislocation, a $\boldsymbol{b_r}$ of $a/6[1\,\bar{1}\,2]_1(1\,1\,1)_1$, and a relatively high $|\boldsymbol{b_r}|$ of 0.41a. The slip–Σ7 GB interaction is shown in Fig. 4b.

For comparisons, we examine slip through a perfect FCC crystal. This can also be denoted as a Σ1 GB as the atomic positions are in coincidental sites across the lattice, thus there is a 0° misorientation in either the [1 1 0] or [1 1 1] plane to construct this boundary. As previously mentioned, since no GB exists in this case, there is no defect structure and 0 GB energy. Of course, the lattice still offers internal friction against slip. Hence the incoming and outgoing slip systems are the same, $a/6[2\,1\,1]_1(1\,\bar{1}\,\bar{1})_1$, and therefore no residual Burgers vector remains in the lattice. The energy barrier to slip transmission is equal to the unstable stacking fault energy, γ_{US}, which is measured to be 254.4 mJ/m^2 for Ni.

4. Discussion

In Section 3, we discuss specific examples of slip–GB interaction and focus on one specific type of GB, the coherent twin boundary, to display the effects of loading orientation and incident dislocation type on the slip–GB reaction. For each slip–CTB and slip–GB case, we measured the dislocation reactions, residual Burgers vector produced during slip transmission, and energy barrier for the process. In this section, we compare the results and show that the magnitude of the residual Burgers vector, $|\boldsymbol{b_r}|$, is proportional to the energy barrier for slip–twin (Section 4.1) and slip–GB (Section 4.2) interaction. Here we analyze two types of materials to show that this trend holds in low (Cu) and high (Ni) stacking fault energy material. Additionally, in Cu, we focus on slip–twin interaction, since Cu has a lower stacking fault energy and thus twinning is more prevalent in this material. Whereas, in Ni, we show that energy barrier versus magnitude of residual dislocation trend is valid for general types of GBs as well, which are seen in typical engineering materials.

4.1. Energetics of slip–twin interaction

In all the slip–CTB cases in Section 3.1, the 30° incident dislocation has a screw and edge component of $a/2\sqrt{2}$ and $a/2\sqrt{6}$, respectively, making it consistent throughout the simulations. As discussed above, once this incident dislocation interacts with the CTB, a twinning partial nucleates at the twin boundary. This twinning partial traverses on the twin boundary and increase the twin thickness by one layer. Here, we note that, dislocation incorporation at the CTB requires an activated twin system at that specific loading direction; other possible interactions involving inactive boundaries are discussed elsewhere [24].

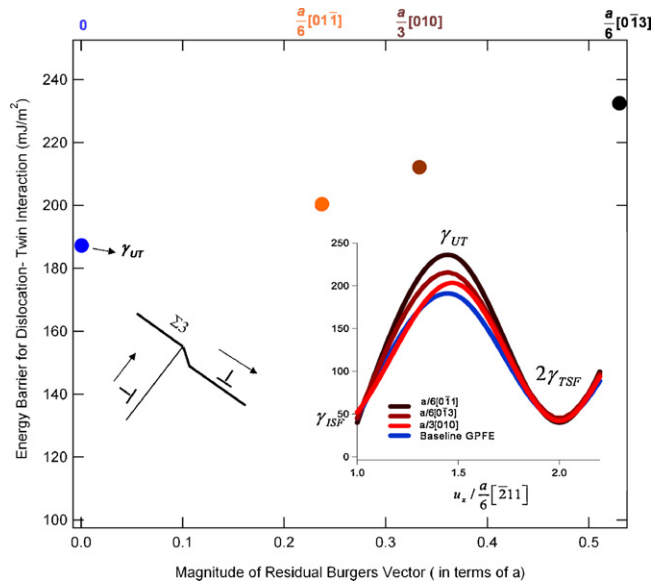

Fig. 5. Plot of the residual dislocation magnitude, $|\boldsymbol{b_r}|$, versus the energy barrier for slip incorporation at the twin boundary in Cu. Cross-slip through a twin produces no residual Burgers vector and its energy barrier is given as the unstable twin energy, γ_{UT}. The complete GPFEs are shown in the (lower right) inset pointing to the effect of the residual Burgers vector. Additionally, a schematic of the stair-rod dislocation formation is shown in the lower left of the image as this process precedes slip transmission through the twin.

During the incorporation process, depending on the direction of the incident and twinning partial dislocations, the magnitude of the residual dislocation left at the twin boundaries alters from 0.23a to 0.52a. This magnitude of residual dislocation during incorporation process is geometric and depends on the acute angle between these two dislocations. The magnitude of residual dislocation and the angle between the incident and the twinning partial are given in Table 2. These residual dislocations are of stair-rod type and situated along the incident dislocation line vector at the twin boundary. By considering their Burgers vectors, it can be seen that every dislocation is of sessile type in character.

The sessile residual dislocations at the intersection enhance the local stress field at the twin boundaries, since it modifies the atomic near neighbor arrangements. The short range planar energy for a dislocation glide is directly influenced by the local stress field around it and reflected by the unrelaxed unstable energy magnitude [32]. A relaxed baseline GPFE (see Appendix A) signifies the energy barrier for dislocation nucleation in the stress free state similar to the simulations conducted in our earlier work using density functional theory [31]. However, the energy barrier can potentially increase or decrease depending on the type of hydrostatic and/or shear loading. Hydrostatic compression (tension) is found to decrease (increase) the unstable energy barrier [38] and a preexisting shear within the dislocation glide plane in the direction of dislocation motion lowers this barrier [39]. With that being said, a residual dislocation at the twin or grain boundary generates a local combined stress field and depends on the geometry and type of residual dislocation. The focus of our results is based on the stress field created by the residual dislocation at the boundary as it increases the energy barrier for slip transmission. Any increase in magnitude of γ_{UT} is due to the presence of stair-rod dislocation and is plotted in Fig. 5. In Fig. 5, the residual dislocation of zero magnitude signifies a cross-slip process that does not leave any residual dislocation at the boundary and the glide energy barrier is given by the baseline γ_{UT}. Hence, screw dislocation-CTB reaction contribution is expected to be small compared to the cases studied here; this difference in energy barrier explains the efficacy of the residual

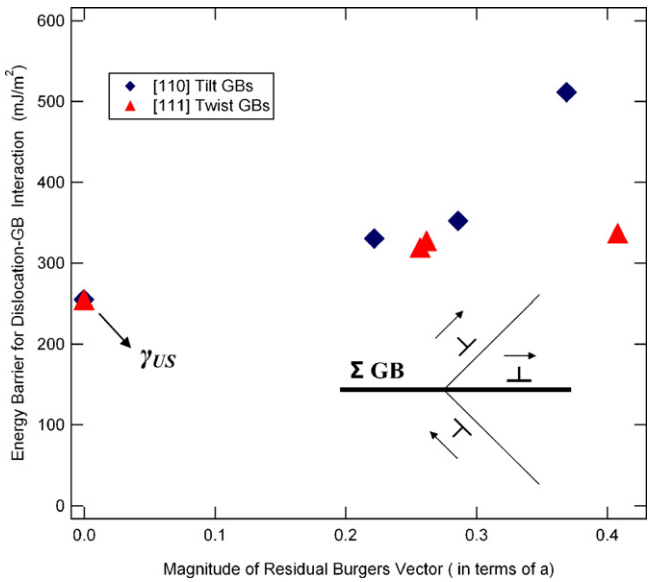

Fig. 6. Plot of the magnitude of the residual Burgers vector $|\boldsymbol{b_r}|$ versus energy barrier for slip transmission for various cases of [1 1 0] tilt and [1 1 1] twist GBs in Ni. For comparison, slip through a perfect FCC lattice is shown as the energy barrier is equivalent to the unstable stacking fault energy of the material, γ_{US}. A schematic of direct transmission through the GB, including a residual dislocation remaining within the GB, is shown in the lower right inset of the image.

dislocation in the hardening process as observed experimentally [13]. However, as discussed above, incorporation at the twin boundary requires a residual dislocation of stair-rod type at the intersection. Geometrically, a stair-rod magnitude varies from a minimum of 0.23a to a value of 0.52a during incorporation. The unstable energy barrier (γ_{UT}) is calculated to vary 6.5–24% from baseline value for the presence of these stair-rod dislocations. Unlike stair-rod dislocations, a Frank partial dislocation creates an angle of 90° with the close packed planes. Hence, the Frank partial dislocation generates a much higher local stress concentration at the barrier. This explains the high 312 mJ/m^2 barrier for the transmitted dislocation near the $a/6[1\,\bar{1}\,1]_T$ Frank partials. The Frank partial is found to increase the unstable energy barrier γ_{US} about 87% higher from baseline γ_{US}. These results point to a significant contribution of the residual dislocations on the energy barriers and ultimately the reaction-induced (complex) stress states at the twin boundaries, which governs the resulting dislocation glide behavior. In addition to the above discussed reactions, Wang and Huang [40] and Deng and Sansoz [41,42] showed that, in nanowires, a dislocation reaction with a twin boundary can nucleate a cube slip on a (0 0 1) plane in the presence of a stair-rod dislocation. This transition in yielding mechanism is due to a lower shear stress magnitude on the regular {1 1 1} glide plane and an excessive image force imposed by the coherent twin boundary. However, dislocation glide on a (0 0 1) plane must overcome a much higher energy barrier [24], and hence, its translation is confined to a short distance and therefore is less observed in bulk material.

4.2. Energetics of slip–GB interaction

As previously discussed, two categories of slip–GB interactions are analyzed, [1 1 0] tilt GBs with cases of Σ1, 9, 11, and 17 GBs and [1 1 1] twist GBs with cases of Σ1, 7, 13 and 21 GB (with the Σ1 simulation referring to slip in a perfect FCC lattice). For each of these cases of slip–GB interactions, the magnitude of the residual Burgers vector, $|\boldsymbol{b_r}|$, and the energy barrier for slip transmission through the GB is recorded and the results are plotted in Fig. 6. For the case of the [1 1 0] tilt GBs, we observe that $|\boldsymbol{b_r}|$ is proportional to the energy barrier for slip transmission. The same trend is observed for the [1 1 1] twist GBs as the energy barrier increases with $|\boldsymbol{b_r}|$. Therefore, slip transmission can readily occur (low energy barrier) in cases, where a low $|\boldsymbol{b_r}|$ is produced during the slip–GB interaction. Adversely, slip transmission is difficult (high energy barrier) resulting in dislocation pile-up and a hardening effect in the material, when a large $|\boldsymbol{b_r}|$ results from dislocation reaction with a GB. Thus, it is imperative to analyze the resulting residual Burgers vector when quantifying the strengthening mechanism of individual GBs. Additionally, it is necessary to distinguish the type of GB character (e.g. [1 1 0] tilt GB or [1 1 1] twist GB), in order for the trend to monotonically hold. This is due to the vast difference in defect structure at the GB between the [1 1 0] tilt versus [1 1 1] tilt boundaries [36,37], which influences the type of residual dislocation that forms within the GB during slip transmission. Thus for the trend to hold, we must analyze similar types of residual dislocations.

The energy barrier for slip transmission through a GB is significantly affected by the character and the structure of the GB, as there is a strong correlation between the energy barrier and interfacial boundary energy. GBs with lower static interfacial energy have a lower density of defects at the GB and thus are inherently stable; as a consequence, these GBs offer a stronger barrier against slip transmission and nucleation at the GB. For example, the Σ11 GB (as shown in Fig. 4a) has a relatively low static GB energy for a [1 1 0] tilt GB [33], and as a consequence its energy barrier for slip transmission is higher than its static GB energy. Similarly, a perfect FCC lattice (Σ1 GB) has no static GB energy, which is significantly less than its energy barrier resisting slip, which is equivalent to the γ_{US}, 254.4 mJ/m^2. For the rest of the GB cases, the static GB energy is higher than the energy barrier for slip transmission, due to the byproduct of the simulation of a defect free bicrystal interacting with only one dislocation. As seen within these simulations, in cases of very high GB energies, the GB is nearly unstable and is prone to dissociation of the GB structure [25]. In real polycrystalline materials, other inherent defects produce stress fields that alter the ability of a dislocation to penetrate the GB and influence the relative energy barriers for slip transmission (such as dislocation–dislocation interaction, compatibility between grains with aggregate, multiple dislocations piling-up at the GB), although the trends reported here still hold true.

In the case of dislocation–dislocation and dislocation–twin interactions, which are prevalent in the literature, slip occurs on closed-packed {1 1 1} planes. The byproduct of these reactions produces well-known structures, such as Frank partials, stair-rod dislocations, Lomer type dislocations, etc. In the cases analyzed in this section, the GB is not a closed pack boundary due to the lack of short-range order, i.e. stacking sequence, at the boundary. Additionally, in many cases, such as [0 1 0] tilt GBs, the GB plane is not a slip plane in FCC materials, {1 1 1}. Due to the lack of a well-defined, close-pack slip plane, there are not simple residual dislocations produced by the slip–GB interaction, such as those reported in classic literature for dislocation–dislocation and dislocation–twin interactions. For this reason, in the case of slip–GB interaction, the residual Burgers vector, $\boldsymbol{b_r}$, presented in Table 3 have Miller indices with large values. Due to the complex nature of the GB structure and the dislocation arrangements within the GB, these atypical dislocation vectors are observed in our simulations and also in experiments [9,10]. Additionally, these $\boldsymbol{b_r}$ represent a step, ledge, or disregistry in the GB plane. Since these GB have a finite thickness, which is typically larger than the length of $\boldsymbol{b_r}$, the step is not always visible. One exception to the atypical dislocation direction of the $\boldsymbol{b_r}$ is the case of slip–Σ7 GB (as shown in Fig. 4b), which produces a $\boldsymbol{b_r}$ that is a partial dislocation (FCC) direction and has been observed experimentally during slip transmission [9,10]. In this case, the Σ7 GB is on the (1 1 1) plane, and the residual dislocation, $a/6[1\,\bar{1}\,2]_1$, on the $(1\,\bar{1}\,\bar{1})$ is a step out of the plane of the (1 1 1) boundary. Thus, the

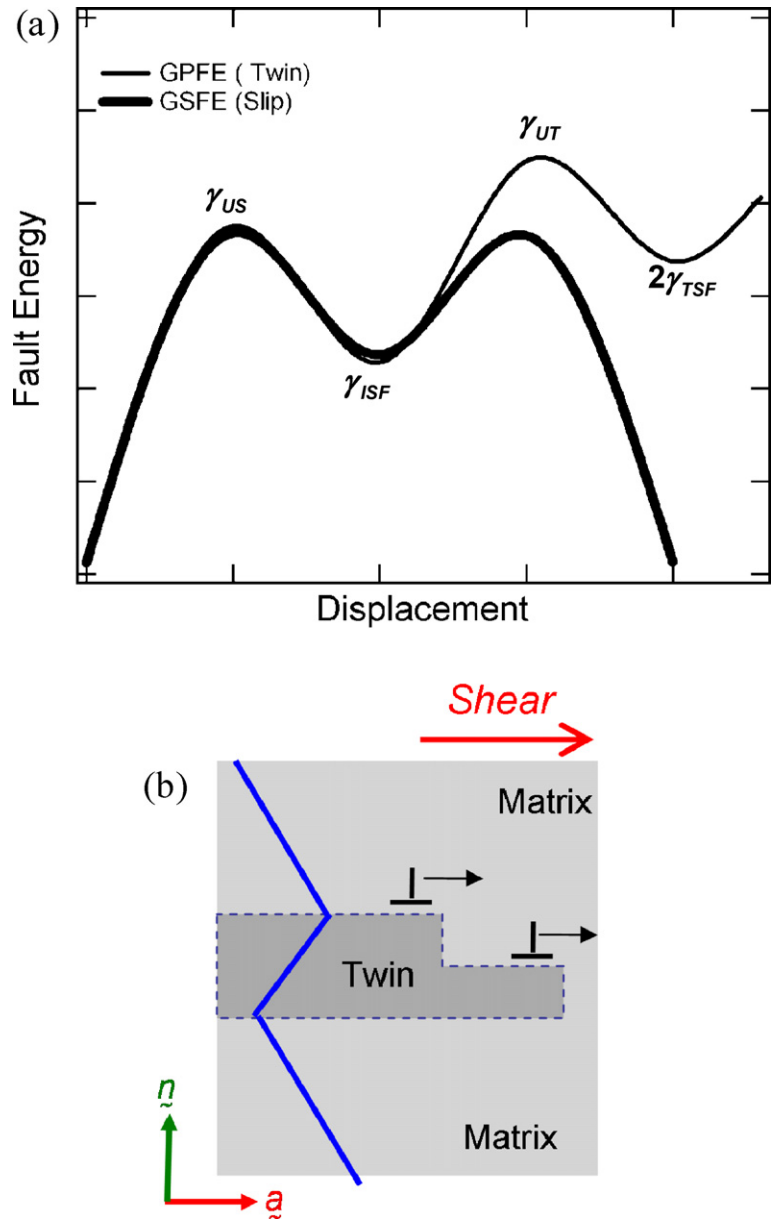

Fig. 7. (a) Schematic of the generalized stacking fault energy (GSFE) and generalized planar fault energy (GPFE) curves are shown with thick and thin black lines, respectively. Energetically significant points such as unstable and metastable positions are labeled. (b) A schematic of the step-by-step twin growth mechanism is illustrated.

notation used to describe $\boldsymbol{b_r}$ in Table 3 is the dislocation direction, which represents a step out of the GB plane.

5. Conclusions

In this study, we have presented MD simulations to systematically analyze slip transmission resulting from slip–twin and slip–GB interactions. This work has outlined considerable progress is characterizing the energy barriers for slip transmission. The seminal result is that the energy barrier for slip transmission is proportional to the magnitude of the residual Burgers vector remaining in the boundary following the dislocation reaction. Additionally, significant contributions of this study are summarized as follows:

- In slip–twin interactions, the barrier provided by the twin boundary is proportional to the magnitude of the residual dislocation. The geometry of the incident dislocation is found to contribute to the value of the residual Burgers vector.
- Loading orientation affects the stress state at the twin boundary; hence, the loading orientation contributes to the direction of the transmitted slip and the magnitude of the residual dislocation.
- In slip–GB interactions, the energy barrier for slip transmission is proportional to the $|\boldsymbol{b_r}|$ for cases of [1 1 0] tilt and [1 1 1] twist GBs analyzed in this study. Here, the type of the GB (i.e. [1 1 0] tilt versus [1 1 1] twist boundaries) is differentiated as this influences the type of residual dislocation remaining within the GB and, as a consequence, the energy barrier for slip transmission.
- The energy barrier is affected by the character and the structure of the GB. The energy barrier for slip transmission is inversely proportional to the interfacial boundary energy. GBs with lower static interfacial energy are inherently stable and consequently offer a stronger barrier against slip transmission.
- Since the GBs are not close-packed planes, the residual dislocation arrangements within the GB plane are complex. The resulting

$\boldsymbol{b_r}$ represent a step or ledge at the GB plane following slip transmission.

Acknowledgments

We note that the authors MDS and TE contributed equally in writing this paper. Support for this work was provided primarily by the National Science Foundation, Virginia, USA, Division of Materials Research, through Grant Number DMR 08-03270. Work of MDS was partially funded by Rolls-Royce Corporation. The authors gratefully acknowledge the use of the parallel computing resource as part of the Turing cluster maintained and operated by the Computational Science and Engineering Program at the University of Illinois.

Appendix A.

In cubic crystal structures, twin formation and growth is aided by a step-by-step glide of the twinning partial. In FCC metals, it is known that a full dislocation splits into partials, since the split dislocations overcome a lower energy barrier, while breaking away as partial dislocations. The generalized stacking fault energy (GSFE) provides a comprehensive description of this energy barrier and describes its possible slip direction. In FCC metals, a full $a/2[1\,0\,\bar{1}]$ dislocation splits into two partial dislocations, a $a/6[1\,1\,\bar{2}]$ leading and a $a/6[\bar{2}\,1\,1]p$ trailing partial, which glide in the same $(1\,1\,1)$ plane. The energy barriers for these two partials are shown with a thick black line in the GSFE curve (in Fig. 7a). During the deformation twin construction, only leading twinning partials nucleate at consecutive planes and generate ledges. This grows the twin perpendicular to the direction of the partial dislocation glide. The mechanism is illustrated in a schematic in Fig. 7b. Barriers for twin formation are usually quantified with the generalized planar fault energy (GPFE) curve (shown with a thin black line in Fig. 7a), which quantifies the energy landscape for twin nucleation in consecutive planes. The point γ_{US} denotes the unstable stacking fault energy. Since a stacking fault is the first step of twin formation in FCC metals, the GSFE and GPFE shares the common energy path up to layer one (point γ_{ISF}). For the cases discussed in Section 3.1, the GPFE is shown in the inset of Fig. 5. Details description of the GSFE and GPFE can be found elsewhere [24].

References

[1] J.P. Hirth, Metallurgical Transactions A (Physical Metallurgy and Materials Science) 3 (1972) 3047.
[2] A.P. Sutton, R.W. Balluffi, Interfaces in Crystalline Materials, Oxford Classical Texts, 2006.
[3] J.P. Hirth, J. Lothe, Theory of Dislocations, 2nd ed., Wiley Interscience, New York, 1992.
[4] L.C. Lim, R. Raj, Acta Metallurgica 33 (1985) 1577.
[5] L.C. Lim, R. Raj, Acta Metallurgica 33 (1985) 2205.
[6] M. Martinez-Hernandez, H.O.K. Kirchner, A. Korner, A. George, J.P. Michel, Philosophical Magazine A (Physics of Condensed Matter, Defects and Mechanical Properties) 56 (1987) 641.
[7] X. Baillin, J. Pelissier, J.J. Bacmann, A. Jacques, A. George, Philosophical Magazine A (Physics of Condensed Matter, Defects and Mechanical Properties) 55 (1987) 143.
[8] W.A.T. Clark, C.E. Wise, Z. Shen, R.H. Wagoner, Ultramicroscopy 30 (1989) 76.
[9] T.C. Lee, I.M. Robertson, H.K. Birnbaum, Philosophical Magazine A: Physics of Condensed Matter, Structure, Defects and Mechanical Properties 62 (1990) 131.
[10] T.C. Lee, I.M. Robertson, H.K. Birnbaum, Metallurgical Transactions A (Physical Metallurgy and Materials Science) 21A (1990) 2437.
[11] J.D. Livingston, B. Chalmers, Acta Metallurgica 5 (1957) 322.
[12] Z. Shen, R.H. Wagoner, W.A.T. Clark, Scripta Metallurgica 20 (1986) 921.
[13] T.C. Lee, I.M. Robertson, H.K. Birnbaum, Scripta Metallurgica 23 (1989) 799.
[14] K.J. Kurzydlowski, R.A. Varin, W. Zielinski, Acta Metallurgica 32 (1984) 71.
[15] Z. Shen, R.H. Wagoner, W.A.T. Clark, Acta Metallurgica 36 (1988) 3231.
[16] A. Jacques, A. George, X. Baillin, J.J. Bacmann, Philosophical Magazine A (Physics of Condensed Matter, Defects and Mechanical Properties) 55 (1987) 165.
[17] X. Baillin, J. Pelissier, A. Jacques, A. George, Philosophical Magazine A (Physics of Condensed Matter, Defects and Mechanical Properties) 61 (1990) 329.
[18] M.E. Gurtin, A. Needleman, Journal of the Mechanics and Physics of Solids 53 (2005) 1.
[19] S. Varadhan, A.J. Beaudoin, C. Fressengeas, Journal of the Mechanics and Physics of Solids 57 (2009) 1733.
[20] J.C. Mach, A.J. Beaudoin, A. Acharya, Journal of the Mechanics and Physics of Solids 58 (2010) 105.
[21] M. De Koning, R.J. Kurtz, V.V. Bulatov, C.H. Henager, R.G. Hoagland, W. Cai, M. Nomura, Journal of Nuclear Materials 323 (2003) 281.
[22] M.P. Dewald, W.A. Curtin, Modelling and Simulation in Materials Science and Engineering 15 (2007) 193.
[23] J.F. Nye, Acta Metallurgica 1 (1953) 153.
[24] T. Ezaz, M.D. Sangid, H. Sehitoglu, Philosophical Magazine 91 (2011) 1464.
[25] M.D. Sangid, T. Ezaz, H. Sehitoglu, I.M. Robertson, Acta Materialia 59 (2011) 283.
[26] S. Plimpton, Journal of Computational Physics 117 (1995) 1.
[27] S. Plimpton, Sandia National Laboratories, 2007.
[28] Y. Mishin, M.J. Mehl, D.A. Papaconstantopoulos, A.F. Voter, J.D. Kress, Physical Review B (Condensed Matter and Materials Physics) 63 (2001) 224106.
[29] S.M. Foiles, J.J. Hoyt, Acta Materialia 54 (2006) 3351.
[30] D.J. Siegel, Applied Physics Letters 87 (2005) 121901.
[31] S. Kibey, J.B. Liu, D.D. Johnson, H. Sehitoglu, Acta Materialia 55 (2007) 6843.
[32] J.R. Rice, Journal of the Mechanics and Physics of Solids 40 (1992) 239.
[33] J.D. Rittner, D.N. Seidman, Physical Review B (Condensed Matter) 54 (1996) 6999.
[34] W. Humphrey, A. Dalke, K. Schulten, Journal of Molecular Graphics 14 (1996) 33–38.
[35] C.L. Kelchner, S.J. Plimpton, J.C. Hamilton, Physical Review B (Condensed Matter) 58 (1998) 11085.
[36] A.P. Sutton, V. Vitek, Philosophical Transactions of the Royal Society of London A (Mathematical and Physical Sciences) 309 (1983) 1.
[37] A.P. Sutton, V. Vitek, Philosophical Transactions of the Royal Society of London A (Mathematical and Physical Sciences) 309 (1983) 55.
[38] X. Dong-Sheng, C. Jin-Peng, L. Ju, Y. Rui, L. Dong, S. Yip, Materials Science & Engineering A (Structural Materials: Properties Microstructure and Processing) 387–389 (2004) 840–844.
[39] S. Aubry, S.P. Fitzgerald, S.L. Dudarev, W. Cai, Modelling and Simulation in Materials Science and Engineering 19 (2011) 065006 (065014 pp).
[40] J. Wang, H. Huang, Applied Physics Letters 88 (2006) 203112.
[41] C. Deng, F. Sansoz, Acta Materialia 57 (2009) 6090–6101.
[42] C. Deng, F. Sansoz, ACS Nano 3 (2009) 3001–3008.